

## Modeling phase variations introduced by extreme broadband dichroics for astronomical photometry

Vinooja Thurairethinam<sup>a,b,\*</sup>, Andrea Bocchieri<sup>c</sup>, Giorgio Savini<sup>a</sup>,  
Lorenzo V. Mugnai<sup>d</sup> and Enzo Pascale<sup>c</sup>

<sup>a</sup>University College London, Department of Physics and Astronomy, London, United Kingdom

<sup>b</sup>UK Astronomy Technology Centre, Royal Observatory, Edinburgh, United Kingdom

<sup>c</sup>La Sapienza Università di Roma, Dipartimento di Fisica, Roma, Italy

<sup>d</sup>Cardiff University, School of Physics and Astronomy, Cardiff, United Kingdom

**ABSTRACT.** The primary requirement of a manufactured optical surface is a combination of an optimized spectral performance to minimize spectral losses and an accurate mathematical definition of its surface form. Variations in the thicknesses of the coating layers of a dichroic beamsplitter can introduce deviations in the observed phase of the reflected and transmitted beams. Here, we use transmission line modeling to explore the effect of high- and low-spatial frequency variations in the thicknesses of the layers to assess the subsequent impact on the resulting phase of the outgoing beams of a dichroic. We apply our methodology to an extreme broadband dichroic designed to comply with the spectral requirements of a dichroic on the ARIEL telescope. We obtain estimates of the expected phase variations when subjected to high- and low-spatial frequency errors in thickness. We show that these non-uniformities introduce a wavelength-dependent shift in the observed phases of the outgoing beam, which may subsequently degrade the point spread function (PSF) using physical optics simulator (PAOS), an open-source, generic Physical Optics Propagation code, to assess the consequent impact on the PSF at the focal plane of the Fine Guidance System 2 (FGS2) photometer.

© 2025 Society of Photo-Optical Instrumentation Engineers (SPIE) [DOI: [10.1117/1.JATIS.11.1.014003](https://doi.org/10.1117/1.JATIS.11.1.014003)]

**Keywords:** space telescopes; dichroic filters; dichroic performance; optical coatings; Monte Carlo simulation; systematics

Paper 24210G received Dec. 7, 2024; revised Feb. 24, 2025; accepted Feb. 27, 2025; published Mar. 18, 2025.

### 1 Introduction

Dichroic filters, or dichroics, are frequently employed on space telescopes to spectrally and spatially manipulate light across different wavelengths, allowing diverse spectra across multiple wavelength bands to be captured simultaneously.<sup>1-3</sup> These optical components act to selectively transmit and reflect predefined wavelengths of light in accordance with the spectral requirements of the instruments toward which these beams are then directed. Typically, they consist of a substrate onto whose surface multilayer coatings are deposited, where the sequence and thicknesses of these layers of coating establish the spectral response of the dichroic through optical interference. The spectral performance on account of this recipe of coatings, as well as the environmental durability, is fundamental to maintaining the efficacy of the dichroic filter. In light of this, the manufacturing process during which the thin film layers are deposited in sequence onto the

\*Address all correspondence to Vinooja Thurairethinam, [vinooja.thurairethinam@stfc.ac.uk](mailto:vinooja.thurairethinam@stfc.ac.uk)

substrate, in particular, the accurate control of the thicknesses of a coating layer, necessitates careful consideration.<sup>4</sup>

These complex dichroic coatings can exhibit phase effects in both transmission and reflection of light, affecting the wavefront error (WFE) and, consequently, the point spread function (PSF) as a function of the wavelength. The deviations in the phase observed across the surface of the dichroic are primarily the result of variations in the thickness of a given coating layer, influenced by the accuracy of the technique and equipment used during the deposition process of the coatings. With regard to the limited precision of the coating equipment, random fluctuations of the thickness across the surface of each coating layer deposition become unavoidable for the manufactured coatings of dichroics. Additional inaccuracies can also stem from the inaccurate termination of the deposition, as well as insufficient sensitivity to detect instabilities in the deposition conditions during the optical monitoring for thickness control.<sup>5</sup> Phase errors are a direct consequence of the modified optical path lengths traversed by light traveling through or reflecting off the coatings due to such altered thicknesses. A dichroic design consisting of parallel-facing smooth coating layers will naturally yield reflected and transmitted beams with homogeneous phases. However, local deviations in the coating layer thickness due to non-uniform depositions can lead to phase variations in the outgoing beams of the dichroic.

A study on the phase shifts induced by a dichroic for the Euclid telescope with non-uniform coating layers was undertaken, and this effect was observed in the form of wavelength-dependent phase shifts.<sup>6</sup> For imaging instruments such as Euclid, such variations can lead to a deterioration in the quality of the image. Similarly, the camera system of the Roman Space Telescope, known as the Wide Field Instrument, contains a filter wheel that was suspected to be susceptible to similar effects, potentially contributing significantly to the overall WFE.<sup>7,8</sup> Moreover, beyond dichroic filters, these coating-induced phase variations have also been observed for mirrors. In a preliminary study of the performance of the Space Infrared Telescope for Cosmology and Astrophysics, the polishing of the primary and secondary mirrors, along with their respective coatings, emerged as leading contributors to the overall WFE budget.<sup>9</sup>

The Atmospheric Remote-sensing Infrared Exoplanet Large-survey (ARIEL) mission aims to perform spectroscopic observations of a large population of known exoplanets.<sup>10</sup> As the mission demands simultaneous observation across extreme wavelength ranges, the necessity for an exceedingly complex broadband dichroic has emerged. As the most complex ARIEL dichroic, D1 comprises over 50 coating layers and will operate at cryogenic temperatures to divide the incident beam of the telescope into two wavebands corresponding to the two instrument modules, the Fine Guidance System (FGS) and the ARIEL InfraRed Spectrometer (AIRS). As illustrated in Fig. 1, this requires the reflection of wavelengths  $0.5 \leq \lambda \leq 1.95 \mu\text{m}$  and the transmission of wavelengths  $1.95 \leq \lambda \leq 7.8 \mu\text{m}$ . Extreme broadband dichroics, such as D1, which consist of a considerable number of coating layers, are prone to non-uniformities at the interfaces of these layers.

## 2 Methodology

This study primarily intends to address a concern regarding the large number of coatings that make up extreme broadband dichroics, such as ARIEL's D1, significantly impacting the phase uniformity of the outgoing beams. As such, this article aims to outline a methodology that can allow the reader to explore the effect of variations in the layer thicknesses, connect them to the subsequent impact on the outgoing beams of a dichroic and the potential effect on astronomical observations. However, the actual design and manufacture of the ARIEL dichroic described in this paper have been entrusted to a commercial supplier.

### 2.1 Modeling Optical Multilayer Coatings

Light reflected and transmitted at the several interfaces of two different media within a multilayer coating structure exhibits variations in phase due to the time taken for light to travel through each of the layers, reflects at the interface, and once again re-enters the previous medium or transmit through to the next medium. The optical thickness of the respective coating layers determines this phase, where the optical thickness is defined as the product of the physical distance that light travels within a given layer and the refractive index of the layer. In this work, we use

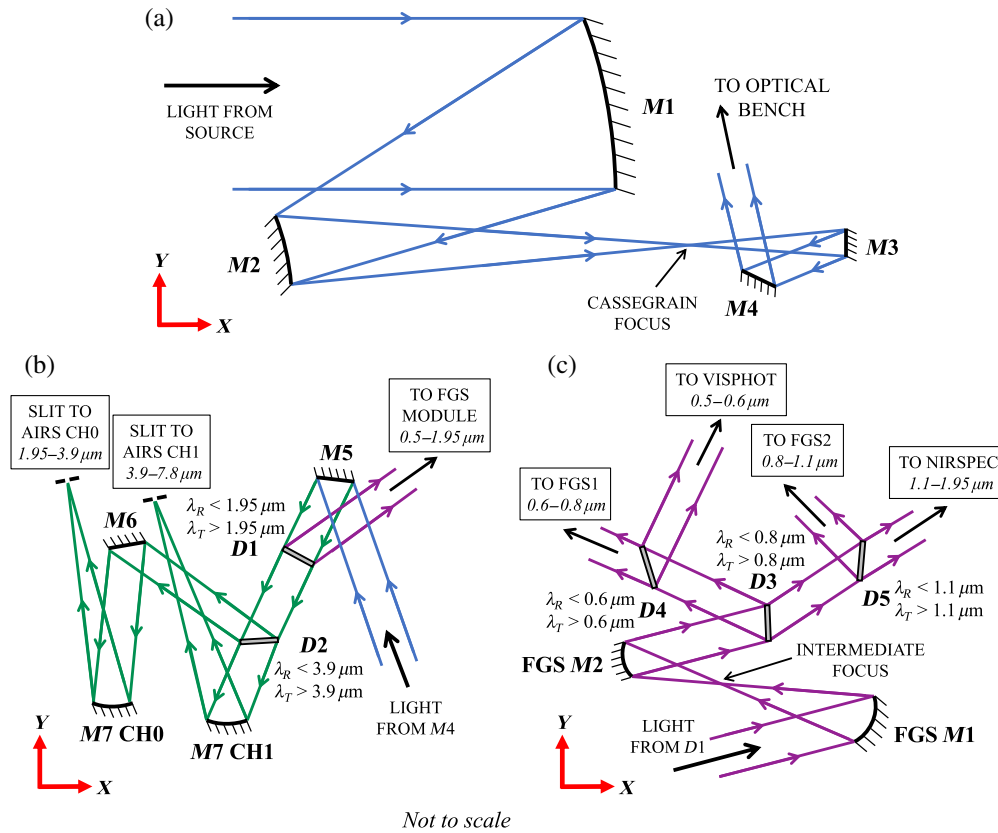


**Fig. 1** Optical configuration of ARIEL and its dichroics. (a) Layout of the ARIEL telescope assembly. (b) Dichroics and mirrors used to separate FGS from AIRS channels. (c) Dichroics and mirrors used to separate the four FGS channels.

our previously developed transmission line modeling tool outlined in Thurairethinam et al.,<sup>11</sup> which has the capability to simulate the performance of a multilayer system, given a recipe of thicknesses, angle of incidence, the polarization of light, and refractive indices, along with other optical material properties including absorption constants. In addition to simulating the optical performance of a defined multilayer system and its sensitivities to various parameters, this tool can also calculate the chromatic phase change experienced by light reflected or transmitted by the optical component.

The recipe of the dichroic is defined as two sets of coating layers deposited on both sides of a substrate consisting of a given set of thicknesses and materials. The detailed recipes of the D1 front and rear coatings have not been published by the manufacturers. It should, therefore, be noted that although the designs of the coatings used throughout this paper are representative of the D1 coating designs, they are not precise replicas. A Monte Carlo (MC) refinement method described in Thurairethinam et al.<sup>11</sup> has been used to fine-tune the parameters, particularly the thicknesses of coating layers, of a starting design until a satisfactory performance in line with the requirements of the component was achieved. The similarity of the coating to the final design results in a performance similar to the design of the D1 dichroic. In light of the comparable performances, it is anticipated that the resulting phase distributions will closely resemble those observed in our present findings and, as such, can be used to estimate the expected phase variations for the dichroic.

## 2.2 Analysis of Variations in Phase

Variations in the phase of light over an individual coating layer surface are heavily influenced by local deviations of the manufactured layer thicknesses from the intended thicknesses in the design of the dichroic. In this context, for an ideal deposition, which by definition has no uncertainty in the thicknesses of the coating layers, there is no phase difference across any specified

surface within the multilayer component. The phase errors resulting from the manufacturing process can be estimated for a level of tolerance provided for the thickness of the coating layers. This tolerance is characterized by the deposition processes of the machine and the limited intrinsic precision to which the specified layer thicknesses are deposited.

The change in phase experienced by a beam transmitted or reflected by a given coating stack can be obtained from the phase of the overall transmission or reflection response coefficients  $\Gamma_C$  and  $\mathcal{T}_C$ . Assuming that there are no backward waves in the exiting right-most medium (i.e.,  $\mathbf{E}_{i+1,-}' = 0$ ), the overall reflection response coefficient  $\Gamma_C$  can be introduced as

$$\Gamma_C = \frac{\mathbf{E}_{1-}}{\mathbf{E}_{1+}}, \quad (1)$$

where  $E_{1+}$  and  $E_{1-}$  are the field amplitudes of the incident and reflected beam, respectively. The reflectance  $R$  can be expressed as

$$R = |\Gamma_C|^2. \quad (2)$$

Similarly, an overall transmission response coefficient  $\mathcal{T}$  may be defined as

$$\mathcal{T}_C = \frac{\mathbf{E}_{N+1,+}' }{\mathbf{E}_{1+}}, \quad (3)$$

where  $N$  is the number of slabs in the component, and  $E_{N+1,+}'$  is the field amplitude of the transmitted beam. The transmittance  $T$  is consequently given by

$$T = \frac{n_s}{n_0} \left| \frac{\mathbf{E}_{N+1,+}' }{\mathbf{E}_{1+}} \right|^2 = \frac{n_s}{n_0} |\mathcal{T}_C|^2, \quad (4)$$

where  $n_0$  and  $n_s$  are the incident and exiting media surrounding the thin film stack.

Hence, for a coating stack  $C$ , the overall phase change of the reflected and transmitted beam,  $\Phi_{R,C}$  and  $\Phi_{T,C}$ , was found using

$$\Phi_{R,C}(\lambda, s_p, \beta_p) = \arg[\Gamma_C](\text{mod } \pi), \quad (5a)$$

$$\Phi_{T,C}(\lambda, s_p, \beta_p) = \arg[\mathcal{T}_C](\text{mod } \pi), \quad (5b)$$

where  $s_p$  and  $\beta_p$  are the radial distance and angular coordinate of point  $p$  on a disk of radius  $r$ , respectively. The overall reflectance of D1 was assumed to be solely affected by the reflectance of the front coating stack of the dichroic. Consequently, the phase change of the reflected beam was determined by the phase change caused by the front coating stack,  $\Phi_{R,\text{front}}(\lambda, s_p, \beta_p)$ . The overall wavelength-dependent phase change experienced by the reflected beam,  $\Phi_R(\lambda, s_p, \beta_p)$ , was therefore defined using Eq. (5a) as

$$\Phi_R(\lambda, s_p, \beta_p) \equiv \Phi_{R,\text{front}}(\lambda, s_p, \beta_p) = \arg[\Gamma_{\text{front}}](\text{mod } \pi). \quad (6)$$

On the other hand, the overall transmittance was defined as a product of the transmission of the front coating stack, substrate, and rear coating stack. These three contributions are not considered to be coherent with each other. The partially reflected and transmitted light within the front coating is coherent, resulting in interference. This is also true for the rear coating. However, due to the substantial thickness of the substrate (1 cm) relative to the wavelength of the beam, there is no coherence within the substrate, so no interference occurs in the substrate. Consequently, to estimate the overall phase change of the transmitted beam, the three individual phase changes experienced by this beam in transmission due to the front coating, substrate, and rear coating were found. At a wavelength of  $\lambda$ , the phase changes of the transmitted light due to the front and rear coating stacks,  $\Phi_{T,\text{front}}(\lambda, s_p, \beta_p)$  and  $\Phi_{T,\text{rear}}(\lambda, s_p, \beta_p)$ , respectively, can be found directly using Eq. (5b) by

$$\Phi_{T,\text{front}}(\lambda, s_p, \beta_p) = \arg[\mathcal{T}_{\text{front}}](\text{mod } \pi), \quad \Phi_{T,\text{rear}}(\lambda, s_p, \beta_p) = \arg[\mathcal{T}_{\text{rear}}](\text{mod } \pi). \quad (7)$$

The phase change of the transmitted light due to the substrate  $\Phi_{T,s}$  was determined by

$$\Phi_{T,s}(\lambda, s_p, \beta_p) = \frac{2\pi}{\lambda} n_s d_s \cos(\theta_s), \quad (8)$$

where  $n_s$  is the real refractive index of the substrate,  $d_s$  is the thickness of the substrate slab, and  $\theta_s$  is the refractive angle of the transmitted beam in the substrate. Therefore, the overall phase change of the transmitted beam of the dichroic,  $\Phi_T(\lambda, s_p, \beta_p)$ , can be found by co-adding the three phase change contributions as follows:

$$\Phi_T(\lambda, s_p, \beta_p) \equiv \Phi_{T,\text{front}}(\lambda, s_p, \beta_p) + \Phi_{T,s}(\lambda, s_p, \beta_p) + \Phi_{T,\text{rear}}(\lambda, s_p, \beta_p) \pmod{\pi}. \quad (9)$$

A manufactured dichroic with variations in the thicknesses of the coating layers will, in turn, result in variations in both  $\Phi_R$  and  $\Phi_T$  from the instance of an ideal deposition. It is the physical distribution of these variations in the overall phase that affects the PSF, rather than the overall phases,  $\Phi_R$  and  $\Phi_T$ , themselves. Taking the  $\Phi_R$  and  $\Phi_T$  to be the reference phase changes of the ideal case, the phase errors,  $\Delta\Phi_R$  and  $\Delta\Phi_T$ , as a result of an altered coating design were computed. This altered design is assumed to have been affected by uncertainty in the thicknesses, and consequently, the resulting variations of the phase change of the beams from their corresponding reference values can be found.

These phase errors illustrate the variation in the phase that may be observed during such a non-uniform deposition process. The variations in the phase for both the reflected and the transmitted beam can be converted to an equivalent WFE for given a wavelength  $\lambda$  using

$$\text{WFE} = \frac{\Delta\Phi}{2\pi} * \lambda, \quad (10)$$

where  $\Delta\Phi$  is the variation from the nominal phase change given in radians.

In the case of D1, an unpolarized beam is incident on the dichroic at an oblique angle. Therefore, the reflectance and transmittance of  $p$ - and  $s$ -polarized light are averaged to obtain the overall spectral performance. This average is done because, in the case of ARIEL, there has not been an expression of interest in the polarization effects themselves. The phase changes  $\Phi_R$  and  $\Phi_T$  for  $p$ - and  $s$ -polarized light will slightly differ from one another. However, this difference among the phase changes experienced by the beam for a given linear polarization state will be an offset. As this paper focuses primarily on the variation in phase from the nominal phase change, the phase of either of the two polarizations can be chosen. The offset among the phase changes for the different polarization is removed when subtracting the reference phase change.

## 2.3 Variations in Coating Layer Thicknesses

Local deviations in the thicknesses of coating layers may manifest with a range of physical sizes, occurring at a range of scales. Subsequently, the effect of these variations on the optical performance of the component is dependent on their spatial frequency. In this study, the deposition errors were categorized as high or low spatial frequency errors, to model their consequent effect on the phase uniformity of the reflected and transmitted beams. In an ideal scenario with parallel-facing smooth coating layers, as shown in Fig. 2(a), the phase remains homogeneous across the surface. This was taken to be the nominal case, where the resultant phase changes of the reflected and transmitted beams served as the reference phase changes.

### 2.3.1 High-spatial frequencies

High-spatial frequency errors pertain to small-scale or short-wavelength imperfections in the profile of the optical surface. These errors stem from the unavoidable random thickness fluctuations across the surface of each coating layer due to the limited precision of the deposition process. This scenario, displayed in Fig. 2(b), assumes that the local deviations across a layer surface are random, attributed to the fact that the repeatability of the deposition process is unknown. High-spatial frequencies essentially manifest as micro-roughness on the surface of a layer, leading to local changes in the spectral response at various points across the surface and affecting phase uniformity.

These random errors were simulated as 10,000 iterations of random fluctuations applied to the thicknesses of the coating layers, representing 10,000 hypothetical points across the physical surface of the dichroic. A ray of light was modeled to pass through each of these points to capture the non-uniformity of the thicknesses of each coating layer. For the matter of this case study, the uncertainty was approximated using the Bühler IBS 1600 tool, which is able to deposit coatings

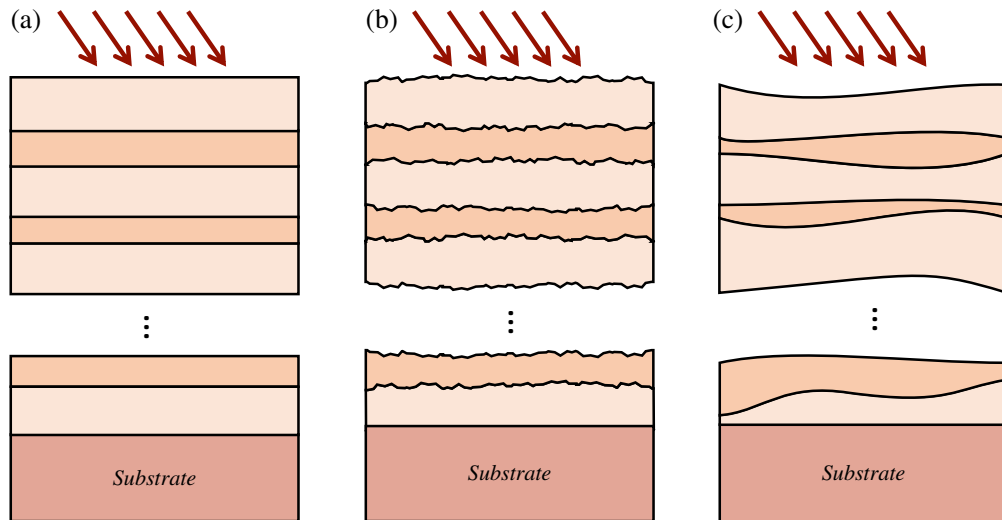


**Fig. 2** Schematic representation of the multilayer model of a coating deposited onto the substrate of the dichroic for various deposition models. (a) Case of ideal deposition, with all layers being smooth and parallel-facing. (b) Case of high-frequency spatial errors in the deposition process. (c) Case of low-frequency spatial errors. In reality, these representative schematics would not be visually discernible from the result of an ideal deposition. The diagrams are exaggerated to emphasize the inherent differences among the models. The arrows show the direction of the incident light.

with a uniformity of  $\pm 0.5\%$ .<sup>12</sup> A ray of light was modeled to pass through each of these points to capture the non-uniformity of the thicknesses of each coating layer. This accounts for the non-uniformity of the phase change at each of these points in comparison with the reference phase change was then found.

**Multilayer scatter losses.** The considerable number of layers that make up D1 will likely result in scattering due to microroughness, particularly for oblique incidence. The surface roughness, quantified using the root-mean-square (rms) roughness, leads to wide-angle scatter, resulting in diffuse losses and, consequently, reduced optical efficiency.<sup>13</sup> The effects of this were modeled with the aim of ascertaining the preservation of the throughput. As such, the angular distribution of the scattered light, which may be simulated using a bidirectional reflectance distribution function estimation, was not considered here. Instead, the scalar scattering equation for the total integrated scatter (TIS) was employed to obtain an estimate of the loss in throughput. For a layer  $i$ , this is given by

$$\text{TIS}_i = 1 - \exp \left[ - \left( \frac{4\pi\sigma_i \cos(\theta_i)}{\lambda} \right)^2 \right], \quad (11)$$

where  $\theta_i$  is the angle of refraction of light in slab  $i$ , and  $\sigma_i$  is the rms roughness.<sup>14</sup> The TIS represents the fraction of the total intensity of the beam that has been lost due to scattering. As demonstrated by Eq. (11), the magnitude of light lost to scattering decreases rapidly with increasing wavelength of light.

Although Eq. (11) readily presents the relationship between the scattering loss and surface roughness, the application of this metric becomes more complex in the presence of multilayers. Rather than directly applying a scattering loss to the final intensity of the reflected and transmitted beams, an iterative routine was implemented. Hereby, the scatter loss was calculated for each layer and applied to the respective Fresnel coefficients. As this fraction of the light is scattered by the coating layer, it no longer contributes to the interference within the multilayer system, so it is removed from the calculation. Defining  $R$  and  $T$  to be the intensities of the reflected and transmitted beams, with the TIS as the fraction of the intensity of the beam that is lost due to scattering, amended Fresnel coefficients, denoted as  $\rho_{i,\text{spec}}$  and  $\tau_{i,\text{spec}}$ , were introduced to describe the behavior of the specular beam. These coefficients are given by

$$\rho_{i,\text{spec}} = \rho_{i,\text{total}} \sqrt{1 - \text{TIS}_i}, \quad (12)$$

$$\tau_{i,\text{spec}} = \tau_{i,\text{total}} \sqrt{1 - \text{TIS}_i}, \quad (13)$$

where  $\rho_{i,\text{total}}$  and  $\tau_{i,\text{total}}$  are the Fresnel coefficients in the absence of microroughness.

This study presents two models, termed the optimistic and pessimistic cases, to illustrate the boundary scenarios for the severity of the total scattering loss. Both of these scenarios have been depicted in Fig. 3. The optimistic case presumes that only the outermost surfaces of the dichroic contribute to the scatter losses of the beam. For reflection, this refers to the incident surface, whereas for transmission, it pertains to the incident and exiting surfaces—the first layer of the front coating and the last layer on the rear surface of the substrate. Conversely, the pessimistic case assumes that, for both transmission and reflection, scatter losses occur at every surface within the coating stack and hence contribute to the overall throughput loss.

To evaluate the magnitude of the scatter loss by a given layer using Eq. (11), an rms roughness must be assigned to the substrate and each of the subsequent coating layers on either side of the substrate. The ZnSe substrate of D1 is expected to have an rms roughness value of 1 nm because it is likely to be subject to polishing. For the coating layers, the rms roughness of a thin film is typically associated with its physical thickness.<sup>15,16</sup> The coatings are considered to consist of alternating layers of ZnSe and YbF<sub>3</sub>.

Wang et al.<sup>17</sup> have measured the rms roughness of a single YbF<sub>3</sub> layer with a thickness of 1600 nm to be 11 nm, corresponding to a deposition temperature of 190°C. Although the deposition temperature for D1 is presently unknown to the author, the rms roughness of the YbF<sub>3</sub> layers is assumed to be 0.7% of their respective physical thicknesses. On the other hand, for ZnSe, Nečas et al.<sup>18</sup> have measured a layer with a thickness of 1173.1 nm to have an rms roughness of 5.9 nm, corresponding to an rms of 0.5% of the thicknesses of the ZnSe layers. These

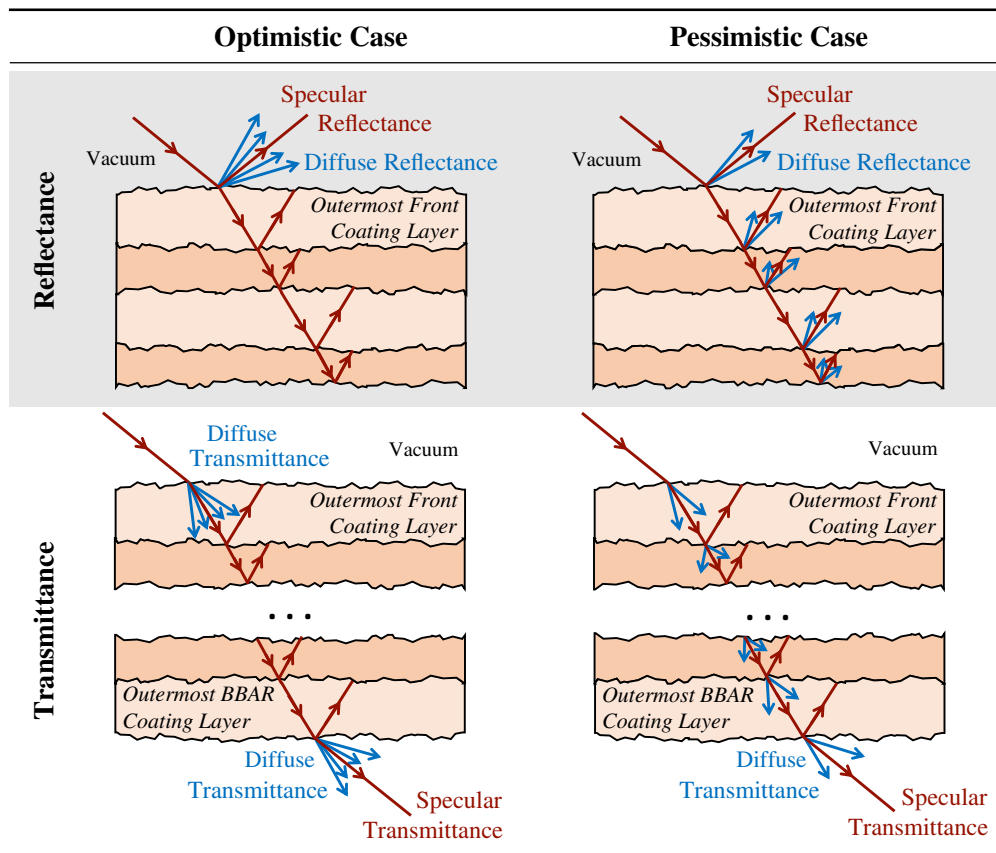


**Fig. 3** Schematic representation of scatter models for both transmission and reflection of a dichroic that consists of a substrate coated on both surfaces.

rms roughness values for both of the thin film materials were used to represent the intrinsic rms,  $\sigma_{\text{int}}$ , of each coating layer.

However, the question remains whether the rms roughness of a given surface within the coating stack is influenced by the preceding layers or stands independent of them. This paper explores three scenarios pertaining to the degree of correlation among the roughnesses of the layers to obtain the effective rms roughness,  $\sigma_{\text{eff}}$ , which is subsequently used to obtain the TIS. Each stack of coatings on either side of the substrate is treated independently, as the form of the layers on either side would not translate through the substrate.

**Uncorrelated.** The uncorrelated model assumes that the rms roughness of each layer within the coating remains independent of the preceding layers within the stack. Thus, the effective rms roughness of a layer is solely determined by the intrinsic rms of a coating layer, such that

$$\sigma_{\text{eff},i} = \sigma_{\text{int},i}, \quad (14)$$

where  $\sigma_{\text{eff}}$  and  $\sigma_{\text{int}}$  are the effective and intrinsic rms roughnesses of the  $i$ 'th layer within the coating stack.

**Correlated.** For the correlated model, the rms roughness of a layer is assumed to be the sum of the roughnesses of all preceding layers, up to and including the layer in question. This also includes the roughness of the substrate on which the layers have been deposited. For a given layer  $i$

$$\sigma_{\text{eff},i} = \sum_{i=0}^N \sigma_{\text{int},i}, \quad (15)$$

where the case of  $i = 0$  refers to the rms roughness of the substrate, and  $N$  is the total number of coating layers on a given surface of the substrate. Hence, the rms roughness of the outermost layers would be equivalent to the rms of the compounded set of layers and substrate below.

**Additive.** The additive case presumes that the rms roughness of a coating layer is given by the sum of squares of the rms of the layers before it, including the layer in question and the substrate. The effective rms roughness of the layer for the additive case is given by

$$\sigma_{\text{eff},i} = \sqrt{\sum_{i=0}^N \sigma_{\text{int},i}^2}, \quad (16)$$

and so, this model effectively calculates the statistical cumulative effect of the roughness from the preceding layers and substrate.

In this way, the 10,000 sets of iterations of random fluctuations applied to the thicknesses of the layers result in slightly altered spectral responses at each point on the surface. Once the relevant scatter loss has been applied, for the 10,000 rays passing through each of these points on the physical surface of the dichroic, the spectral response at each point is found. These rays are combined incoherently to determine the overall spectral transmission and reflection of the dichroic.

## 2.4 Low-Spatial Frequencies

Low-spatial frequency deviations in the surface form can be described as large-scale errors, indicating gradual changes in the surface profile over large spatial regions, as shown in Fig. 2(c). In contrast to high-spatial frequency errors, the primary concern of low-spatial frequency defects is their effect on resolution, rather than throughput. Figure errors resulting from inaccuracies in the manufactured form from its intended mathematical definition primarily lead to conventional aberrations.<sup>13</sup> These form errors tend to affect the peak-to-valley (PtV) and rms WFE of the beam, stemming from a prominent systemic error in the deposition process.

The form errors are considered to take the form of a first-order or second-order polynomial in the thickness of each coating layer. Subject to the configuration of the deposition machine and process, these thickness gradients may vary. In the case of a rotating substrate during deposition, these gradients may be reoriented for each layer, whereas in the absence of such rotation, the gradients may be aligned along the same orientation across all coating layers. The circumstance wherein no reorientation occurs is regarded as the potential worst-case scenario, as this causes

the systematic errors of the layer thicknesses to progressively compound, further exacerbating the overall form deviation of the dichroic.

To illustrate such a form error, D1 was modeled as a circular disk of radius 16.5 mm. In the case of a form error as a systematic thickness deposition error, the modified thicknesses were all subject to a consistent thickness error of  $\Delta d = +0.5\%$  for each layer within the stack. The orientation of the gradients for each coating layer can either be chosen to be random or constant with respect to the other layers within the stack. During the deposition process, substrates are often set up to rotate to aid with coating uniformity. Thus, for the purpose of this study, the gradients within the thicknesses of the coating layers have been considered to be randomly oriented within the stack. Given these form errors, the total phase changes for a grid of points on the surface were then calculated based on the resulting altered recipe of thicknesses at each point. Thus, the thicknesses of a layer  $i$  at a given point  $p$  in the surface of the dichroic, as a result of low-spatial frequency errors, were modified as follows

$$d_{p,i} = d_i + \delta d_{p,i}, \quad (17)$$

where  $d_i$  is the designed thickness of the layer, and  $\delta d_{p,i}$  is the change in the thickness of the layer as a result of a form error. This was then used to compute a phase map for the simulated dummy dichroic.

#### 2.4.1 First-order polynomial

In the presence of a first-order gradient, the dichroic will assume the form of a wedge, with the incident layer exhibiting a more pronounced overall gradient. A first-order polynomial gradient was introduced using a random angle,  $\alpha$ , for each layer, generated from a uniform distribution ranging from 0 to  $2\pi$  radians. The thickness of a layer at a given point  $p$  on the surface is specified by applying a change in  $\delta d_{p,i}$  to it. This change in thickness at a point  $p$  on the surface of the  $i$ 'th layer is given by

$$\delta d_{p,i} = \frac{s_p}{r} \times \cos(\beta_p - \alpha) \times \frac{d_i \Delta d}{2}, \quad (18)$$

where  $s_p$  and  $\beta_p$  are the radial distance and angular coordinate of point  $p$  on a disk of radius  $r$ . Equation (18) is employed to introduce a gradient across the surface, where the direction of this gradient varies randomly among each layer, and its magnitude depends on the thickness of the layer. The magnitude of the gradient spans from  $-\frac{\Delta d}{2}$  to  $+\frac{\Delta d}{2}$  at two opposing ends of the disk, resulting in an overall range of  $\Delta d$  in the change of the thickness of each layer.

#### 2.4.2 Second-order polynomial

The second-order polynomial relies on a similar model. In the instance of a second-order form, rather than an angle, five random coefficients, denoted as  $c_{1,i}$  to  $c_{5,i}$ , are generated for each layer  $i$  from a uniform distribution spanning from  $-1$  to  $1$ . Following this, the two-dimensional quadratic function  $f$  has the form

$$f_{p,i} = c_{1,i}x_p^2 + c_{2,i}y_p^2 + c_{3,i}x_p y_p + c_{4,i}x_p + c_{5,i}y_p, \quad (19)$$

where  $x_p$  and  $y_p$  are the Cartesian coordinates of a point  $p$  on a surface with the origin defined to be at the center of the disk, and  $c_{1,i}$ ,  $c_{2,i}$ ,  $c_{3,i}$ ,  $c_{4,i}$ , and  $c_{5,i}$  are constants. By dividing this by the range of  $f_{p,i}$  followed by subtracting the mean of  $f_{p,i}$ , the second-order form can be normalized and shifted to be approximately symmetrical in the  $f = 0$  plane. Therefore, the change in thickness can be found using

$$\delta d_{p,i} = \left( \frac{f_{p,i}}{\max(f_{p,i}) - \min(f_{p,i})} - \bar{f}_{p,i} \right) d_i \Delta d, \quad (20)$$

where  $\max(f_{p,i})$  and  $\min(f_{p,i})$  are the maximum and minimum of the second-order function, and  $\bar{f}_{p,i}$  denotes the mean.

## 2.5 Impact on ARIEL Observations of Stellar Targets

The optical effects of D1 will propagate through the optical chain of the ARIEL telescope and have subsequent effects on the observations of targets at the various focal planes of FGS and AIRS. To investigate the potential effects on ARIEL observations, the software ExoSim 2.0 was employed.<sup>19</sup> ExoSim 2.0 is a time-domain simulator for exoplanet observations developed for the ARIEL mission and is capable of generating focal plane images of stars akin to those observed by ARIEL during operation. This is achieved by modeling the modification of the stellar signal as it traverses through the optical system to the detectors of any photometric and spectroscopic channels. Therefore, it can propagate the influence of the previously investigated systematics on the performance of D1, extended to the astrophysical observations of the ARIEL targets.

The stellar sources in ExoSim 2.0 can be simulated using the PHOENIX synthetic stellar spectra, which were automatically selected from a number of .fits.gz files for a given stellar radius, stellar mass, effective temperature, distance, and metallicity. Selected from a list of potential ARIEL targets presented in Edwards et al.,<sup>20</sup> the star HD 209458 is used as an example for the purpose of demonstrating the effects of these systematics on the observation of a source, where the relevant stellar parameters were obtained from Boyajian et al.<sup>21</sup> HD 209458 is an F-type star orbited by its planet HD 209458 b, a gas giant, which has been found to be suitable for study in transit with the ARIEL telescope (Fig. 4).

ExoSim 2.0 generates a monochromatic PSF in the form of an Airy disk for each wavelength within the respective wavebands of the channel and multiplies this PSF by the intensity of the source signal at the corresponding wavelength. The result is applied to the respective pixels of the detector. In the case of a spectrometer, this process produces a dispersed image of the spectrum, whereas for a photometer, the PSFs are co-added to create the final photometric image. In practice, the irradiance is not solely affected by the stellar source; another source of astrophysical light between the light source and the telescope includes zodiacal light. However, as the aim of this paper is to investigate the effect of optical effects of the D1 dichroic, no zodiacal foreground has been modeled here. With the complete absence of these foregrounds, the image of the star on the focal plane should be determined solely by the quality of the telescope optics and by the diffraction of light. This allows for the isolation of any optical effects.

In addition, the simulations focus solely on ideal pointing conditions without the inclusion of any pointing offsets induced by jitter, such that the telescope is pointed directly at the coordinates of the target. Moreover, all sources of detector noise have been deliberately omitted. This allows any effects resulting from changes in the performance of D1 to be isolated and easily identified. In this context, such a detector implies that in the absence of any illumination, no signal should be detected.

### 2.5.1 FGS2

To demonstrate the impact of D1 phase non-uniformities on the observations conducted by ARIEL, we focus on the photometric channel FGS2, which has the function of centering,

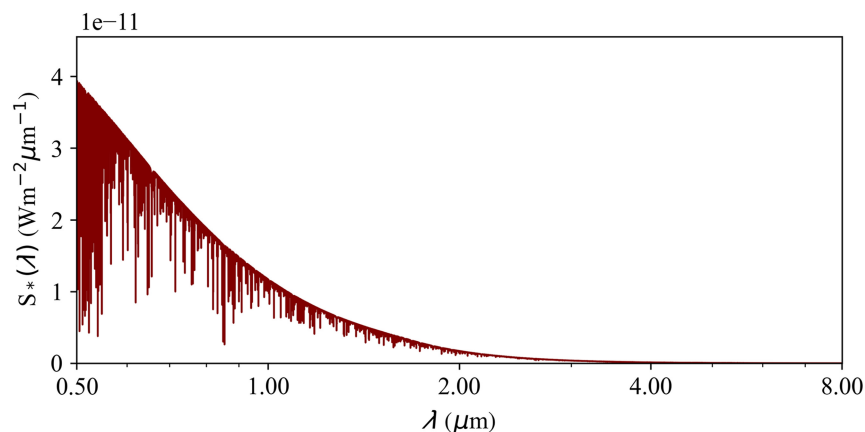


**Fig. 4** Stellar flux densities as a function of wavelength of the selected target, HD 209458, plotted on a logarithmic wavelength scale.

focusing, and guiding the spacecraft. The simulated detector of FGS2 is oversampled by a factor of 3, allowing for the use of subpixels, where a factor of 3 implies that each whole pixel is subdivided into a grid of  $3 \times 3$  subpixels. This oversampling was required when fitting a Gaussian to the PSF of the photometric channel. ExoSim 2.0 convolved the spectrum of the light source with the oversampled 2D PSF as a function of wavelength. Although this PSF can be specified as an Airy disk, ExoSim 2.0 also allows for a custom PSF to be imported. For the case of FGS2, a simulated PSF was obtained from physical optics simulator (PAOS), an end-to-end physical optics propagation simulator designed specifically for ARIEL and its optics.<sup>22</sup> It enables the user to simulate the propagation of the complex wavefront through the ARIEL optical system, thereby producing a PSF at the focal plane of FGS2.

Low-frequency variations in the thicknesses of the layers of the D1 coating can impact the phase uniformity of the beam that is reflected toward the FGS instrument. By extension, this affects the WFE and, consequently, the PSF as a function of wavelength. This can potentially degrade the image quality of the PSF at the focal plane of FGS2. By computing these phase maps for all wavelengths in the FGS2 wavelength range, the subsequent WFE maps were generated and propagated through the ARIEL optical chain to the FGS2 focal plane using PAOS. With this, the PAOS PSFs could be imported into ExoSim 2.0, and the consequent impact on the derived centroid position of the photometric image of the FGS2 photometer was investigated.

### 3 Results and Discussion

#### 3.1 Modeling Optical Multilayer Coatings

The simulated overall reflection and transmission of a D1-like dichroic were modeled from an unpolarized incident beam of light at a given angle of incidence to a multilayer structure composed of thin-film coating layers of specified thicknesses with given refractive indices. Further information on the detailed modeling and design process is beyond the scope of this paper and can be found in Thurairethinam et al.<sup>11</sup> Figure 5 shows the spectral profile of the optimized D1-like design at a temperature of 50K for an angle of incidence of 12 deg obtained from the MC simulation. This design of D1 consists of a front coating of 55 layers and a rear coating of 11 layers, with alternating layers of  $\text{YbF}_3$  and ZnSe, the thickness of which are a unique non-quarter-wave fractional thickness to reduce ripple amplitude. The design aims to have a high

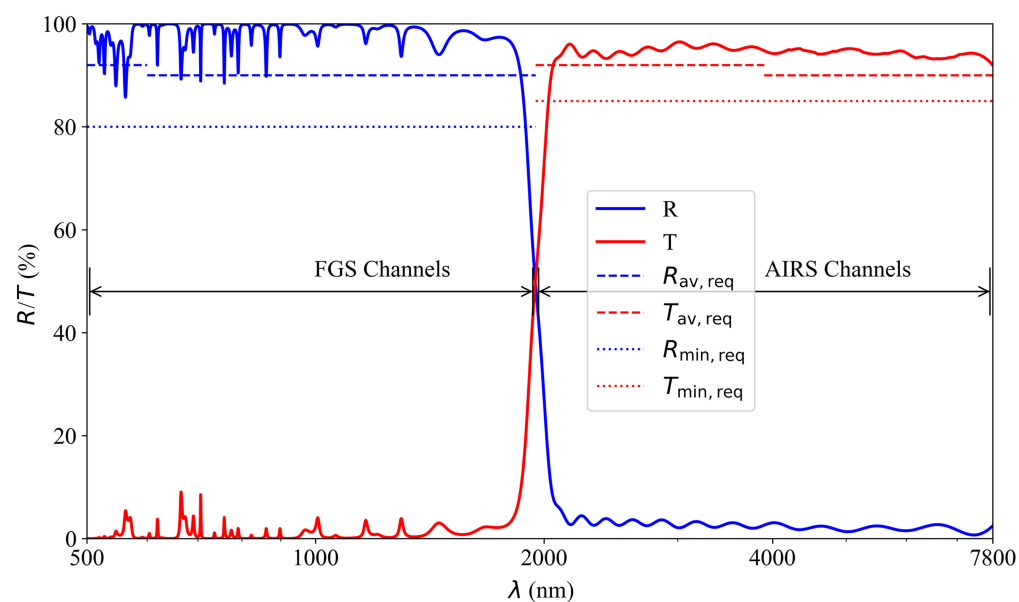


**Fig. 5** Spectral profile of the D1-like dichroic design at an angle of incidence of 12 deg, on a logarithmic wavelength scale. The simulated reflection,  $R$ , and transmission,  $T$ , are plotted as solid red and blue lines, respectively. The respective dashed lines indicate the average required performance,  $R_{av,req}$  and  $T_{av,req}$ , whereas the dotted lines represent the minimum performance requirements,  $R_{min,req}$  and  $T_{min,req}$ .

reflectance at  $\lambda < 1950$  nm while aiming for high transmittance at  $\lambda > 1950$  nm. The spectrum shows a high reflectance and high transmittance within the required regions, with a number of interference fringes visible at lower wavelengths of the stopband. The transition from the stopband to the passband also closely matches the requirement of  $\lambda \approx 1950$  nm with the purpose of separating the incoming beam for the FGS and AIRS instruments.

### 3.2 Coating Thickness Versus Phase Errors

The comparison of the phase errors resulting from high-spatial frequency irregularities within the layer thicknesses and those arising from low spatial frequency variations is shown in Fig. 6. The high-spatial frequency deviations were modeled as 10,000 points on the surface of the dichroic for which the thicknesses had randomly been altered within a given tolerance  $\pm\Delta d$ . This yields differences in the expected phase due to effectively 10,000 sets of randomly varied recipes, resulting in phase errors that exhibit a generally Gaussian distribution.

Although the scatter plots of Fig. 6 present the distribution of phase errors, the histograms fitted with a Gaussian curve show the deviations in phase. The high-spatial frequency variations were generated from a Gaussian distribution, defined using a mean of zero and a standard deviation of  $\Delta d$ . In this way, the resultant deviations in the thicknesses may be positive or negative and fall below or just beyond  $\pm\Delta d$ . The maximum extent of each distribution remains largely symmetric around the nominal phase at which  $\Delta\phi = 0$  and appears to scale linearly with the value of  $\Delta d$  for the reflected and the transmitted beams at  $\lambda = 1.1 \mu\text{m}$  and  $\lambda = 5 \mu\text{m}$ . As the magnitude of the random variations of the thicknesses increases with  $\Delta d$ , the optical path lengths traversed by light also increase in direct proportion. Hence, this leads to an increase in the extent of the phase errors observed for both the reflected and transmitted beams. Moreover, the positive gradients apparent in the distributions of the scatter plots highlight the correlation between the change in the total thickness coating stack and the resulting phase errors.

The direct relation between deviations in layer thickness and the resulting phase error becomes most evident when considering the thickest layer within a coating stack. If a relative

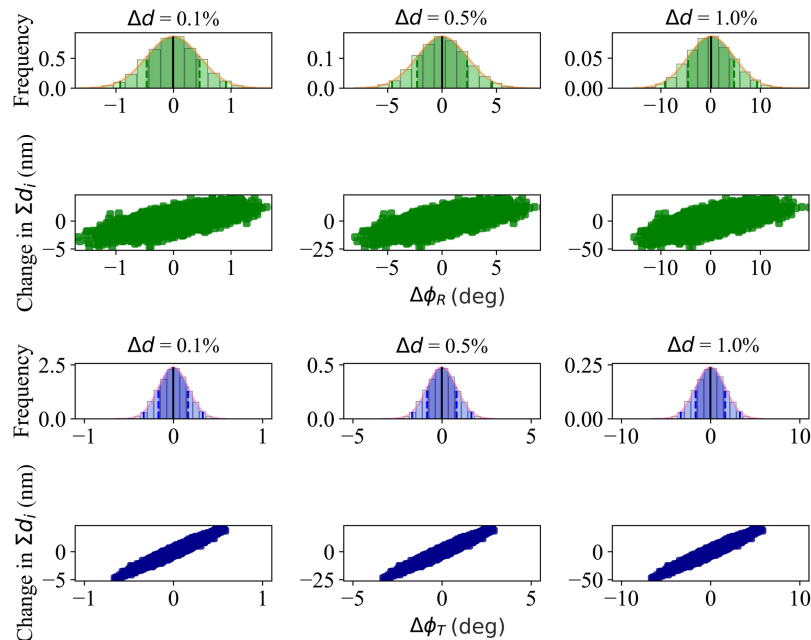


**Fig. 6** Distributions of phase errors due to high-spatial frequency variations for the reflected beam at a wavelength of  $1.1 \mu\text{m}$  in green and for the transmitted beam at  $5 \mu\text{m}$  in blue, for a range of tolerances on the thickness. The scatter plots show the total thickness of front and rear coatings and the resulting phase error from the 10,000 sets of randomly varied recipes. The histograms depict the phase difference distributions as a result of a given  $\Delta t$ , with a Gaussian curve fitted to each histogram. A black vertical line marks the calculated mean of the distribution,  $\mu$ , whereas the dashed vertical lines in the histograms indicate the levels of one and two standard deviations.

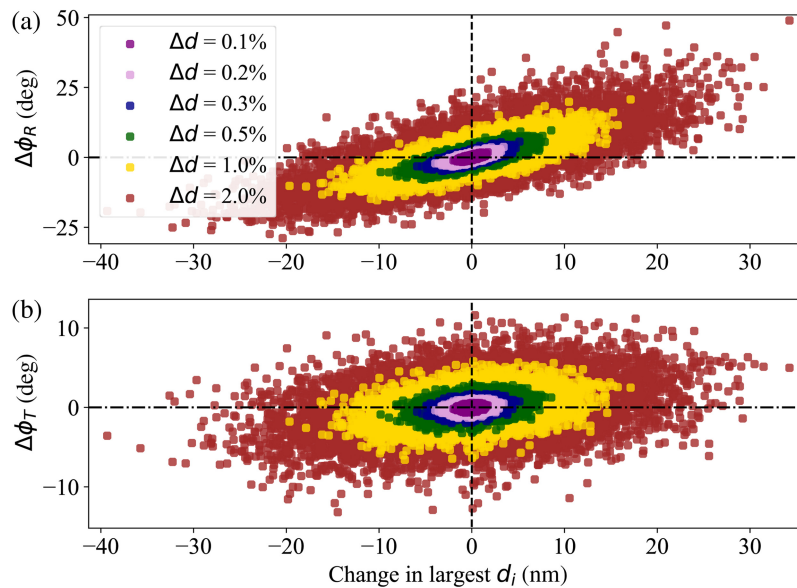


**Fig. 7** Total phase errors due to high-frequency spatial variations in the thicknesses of coating layers in the form of 10,000 sets of randomly varied recipes as a function of the altered thickness of the thickest layer in the coating stack. The upper plot shows the case of the reflected beam at  $1.1 \mu\text{m}$ , whereas the lower plot shows the phase errors of the transmitted beam at  $5 \mu\text{m}$  for a range of values of  $\Delta d$  applied to the thicknesses of the layers. The vertical dashed black lines mark the designed thickness of the thickest layer, and the horizontal dashed lines mark  $\Delta\phi = 0$ .

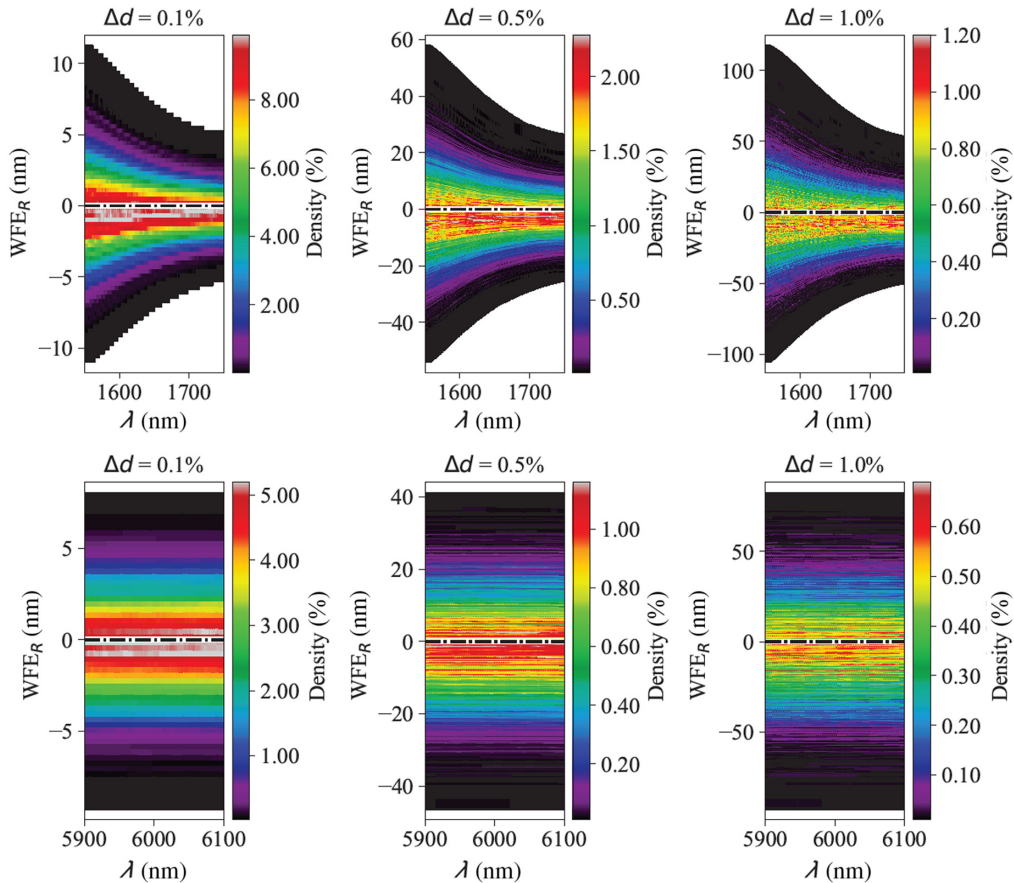
thickness error  $\Delta d$  is applied to a coating layer of substantial thickness, it will cause a more pronounced alteration in the thickness of this layer and, in turn, the overall total thickness of the coating. Thus, the presence of a thick coating layer will significantly impact the total optical path difference traversed by the beam and, ultimately, the overall phase error. This is the case for both low- and high-spatial frequency surface variation.

Figure 7 depicts a scatter graph of the total phase error arising from the randomly varied recipes due to a high-spatial frequency error in the thickness and the subsequent changes in the thickness of the largest layer of the coating. For both the reflected and the transmitted beam, Fig. 7 shows a positive correlation, demonstrating the dependency of the phase change of the beam on the layer with the largest physical thickness. This association is more pronounced for the reflected beam, where a steep gradient can be observed, further demonstrating that the reflected beam is more sensitive to variations in coating layer thickness. Increasing the layer thickness leads to an increase in optical path length, resulting in a positive phase error. Conversely, a decrease in the thickness and, thus, a reduced optical path length results in a negative phase difference. This takes the form of a positive correlation in Fig. 7. In addition, as illustrated in Fig. 6, the extent of the change in layer thickness expands with  $\Delta d$ ; consequently, the range of the observed phase error also increases.

### 3.3 Chromatic Wavefront Dependencies

Errors in phase create equivalent deviations in the wavefront, in the form of a WFE. Two sections of the waveband within the high reflection and the high transmission regions of D1 were selected to examine the wavelength dependence of the WFE. The wavelengths were selected to be regions where the spectral performance of the design obtained in this paper most closely resembles the expected performance of the ARIEL D1 dichroic. The WFEs stemming from high spatial frequency deviations in the thicknesses of coating layers at 10,000 non-localized points were calculated for each wavelength. The contoured two-dimensional histogram displayed in Fig. 8 showcases the extent of potential WFEs observed in the reflected and transmitted beams, along the most likely range of WFEs that may be observed for each wavelength.

For both the reflected and transmitted beams, the plots show a smooth gradient centered around the WFE = 0 axis, indicated by the dashed black line. This gradient extends outward



**Fig. 8** Contoured two-dimensional histogram of the 10,000 sets of random thickness errors for a range of wavelengths where the performance of our design was deemed the most representative of the D1 spectrum. The same 10,000 sets of randomly generated recipes were used to compute the resulting wavefront errors of the coating at each of these wavelengths. The color bar indicates the density percentage of the WFEs of each bin, where the bin width is 0.3 nm. Wavelength regions of the high-reflectance band are plotted in the upper row, and those within the high-transmittance band are plotted in the lower row for various values of  $\Delta d$ . A dashed black line marks where the wavefront error is zero.

along the positive and negative WFE directions in a relatively symmetrical manner at each wavelength, with a distribution resembling a Gaussian curve. Moreover, the extent of the possible WFEs for the transmitted and the reflected light once again scale approximately linearly with the value of  $\Delta d$  owing to the established correlation between  $\Delta d$  and the optical path length. In this way, as  $\Delta d$  decreases, the extent of the WFEs also decreases. The bin widths have been chosen to remain constant while varying  $\Delta d$ , and the resolution of the contoured histograms decreases accordingly.

The range of WFEs for a given  $\Delta d$  differs between the reflected and transmitted beams. In the case of the reflected beam, this range decreases with increasing wavelength, whereas for the transmitted beam, the range remains constant throughout the different wavelengths. This can be explained by referring to Fig. 5 and noting the several interference fringes within the high reflection band, compared with the mostly steady transmission performance in the high transmission band. In the region of high reflection at wavelengths just below  $1.55 \mu\text{m}$ , rapid fluctuations occur in the reflectance due to an interference fringe, whereas at wavelengths just above  $1.75 \mu\text{m}$ , the reflectance remains relatively stable. Any variations in the thicknesses of the layers will result in changes in the observed interference. This results in a less stable performance and, consequently, a wider range of WFEs. Conversely, at most wavelengths in the high transmittance region, the transmission continues to be stable with a relatively flat spectral response. Hence, the random variations in the layer thicknesses will have a much more subdued impact on the transmission,

resulting in a consistent range of WFEs. Considering the maximum extent for a scenario of  $\Delta d = 1\%$ , the WFEs for both reflection and transmission remain relatively small in comparison with their respective wavelengths.

### 3.4 High-Spatial Frequencies: Scattering Losses

The nominal spectral performance shown in Fig. 5 is likely to be affected in the presence of high-spatial frequency errors due to scattering losses. The extent of these losses was explored for two boundary case models to estimate the magnitude of scattering within multilayer structures. The magnitude of this scattering loss is strongly reliant on the degree of correlation of the micro-roughness of the individual coating layers. Figure 9 presents the effective rms roughness of each layer for each of the models simulated, whereas Fig. 10 shows plots portraying the spectral response for each of these scenarios in both reflection and transmission.

In the case of the optimistic scatter model, shown in Figs. 10(a) and 10(b), only the outermost layers contribute to the observed scatter losses. Regardless of the models of surface roughness correlation applied, the change in the spectral response of the dichroic remains negligible for both the transmitted and reflected beams. This behavior can be interpreted through Fig. 9 by referring to the effective rms microroughness  $\sigma_{\text{eff}}$  of the exterior layers of the front coating and the rear coating stack. In the optimistic scenario, the loss in intensity due to the scattering of the reflected beam is determined by the external layer of the front coating, whereas the outermost layer of both the front and rear coating impacts the intensity loss of the transmitted beam. The performance remains largely unaffected by an uncorrelated roughness correlation, with the expected rms roughnesses of both of the outermost layers assuming the intrinsic roughness of the deposition of their respective materials. Similarly, with an additive roughness correlation among coating layers, both of the exterior layers adopt a relatively small  $\sigma_{\text{eff}}$ . Considering a correlated rms surface roughness model, the rms roughness of the external layers is represented by the cumulative sum of the rms roughnesses of the precedent layers. As only the outermost layers are considered to contribute, for the optimistic case, the losses for all three correlation models remain negligible.

On the contrary, when considering the pessimistic scatter model displayed in Figs. 10(c) and 10(d), all layers within the coating stack are now considered to contribute to the intensity losses of the beam due to scattering. As is the case with the optimistic model, the scatter losses remain negligible when considering the uncorrelated surface roughness, albeit slightly larger. However, with an additive correlation of the rms roughnesses, the magnitude of the losses increases slightly in reflection, and a loss can also be observed in transmission at the shorter wavelengths of the passband. This loss further increases to rather considerable levels in the case of a correlated rms

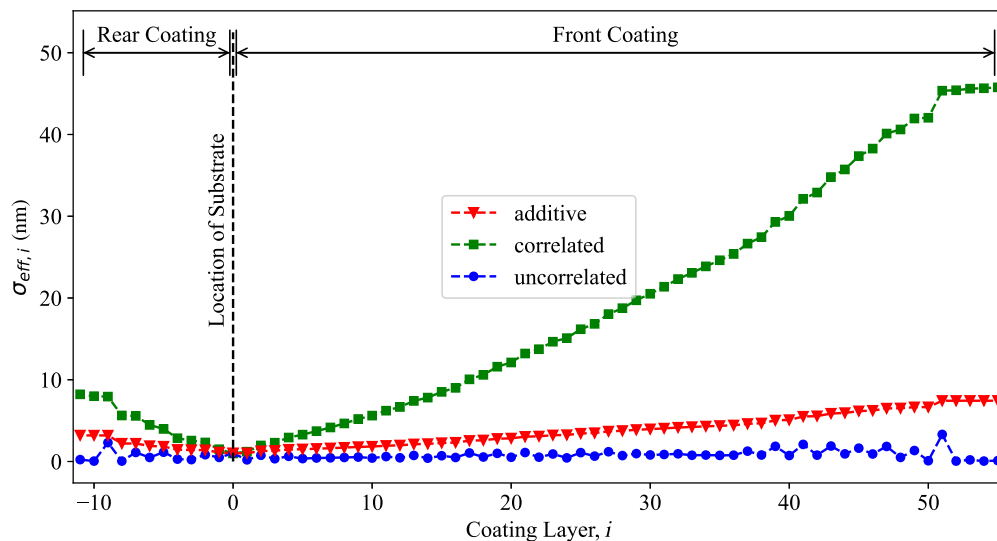


**Fig. 9** Effective rms roughness for three models of roughness rms correlation among the coating layers. The substrate location is indicated at  $i = 0$ , and the remaining interfaces are numbered in order of deposition, with rear coating layers assigned negative values.

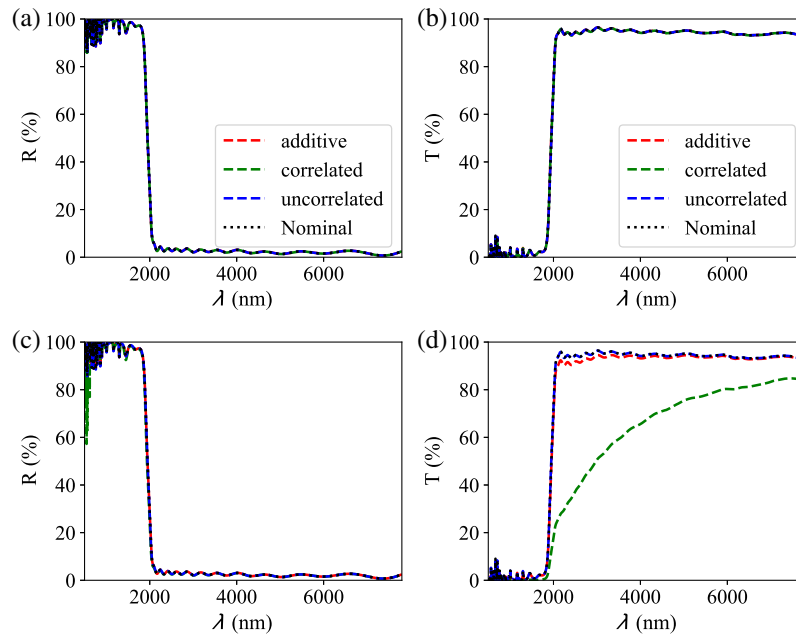


**Fig. 10** Expected changes in spectral performance due to scatter losses. (a) and (b) Specular reflectance and transmittance for the various rms roughness correlations in the case of the optimistic model. (c) and (d) Specular reflectance and transmittance of the pessimistic model.

roughness model for both the reflected and the transmitted beam. The rapid increase in the effective rms roughness of each layer within the front coating leads to a large loss in the spectral performance in the transmission where the exponential effect of Eq. (11) is increasingly apparent. In addition, in line with Eq. (11), the loss in intensity is more pronounced at shorter wavelengths. Based on the large number of coating layers, with losses assumed to occur at each of these surfaces, there exists a strong correlation between the number of coating layers and the degree of loss from scattering.

### 3.5 Low-Spatial Frequencies: Spatial Patterns in Phase Errors

Phase error maps were simulated for the D1-like dichroic to study the effects of low-spatial frequency thickness variations on the distribution of the phase errors across the surface of the component. Deposition gradients of first- and second-order were modeled as randomly varied gradients applied to each of the coating layers, assuming a deposition machine sensitivity of  $\Delta d = 0.5\%$ . In the case of a first-order gradient systematic in the thickness of the coating layers, the front and rear coatings assumed a slight wedge shape as a result of the randomly oriented thickness gradients of each layer, with an overall gradient across the external surfaces of the coating. Similarly, a number of second-order polynomials collectively produce an overall second-order form across the external surfaces of the coating. The resulting phase error maps of the reflected and transmitted light at a number of wavelengths in light of these altered coating thicknesses were found. The wavelengths were chosen based on the stability of the spectral performance of the nominal coatings, with wavelengths that exhibit relatively stable spectral performance with minimal features,  $\lambda_{\text{stable}}$ , as well as wavelengths where the spectrum shows fringes or ripples in the spectral response,  $\lambda_{\text{unstable}}$ .

For the first-order gradient in the thicknesses, the various resulting phase error maps display smooth gradients oriented in different directions. As the thicknesses of the layers are altered in a symmetrical manner, the subsequent phase errors for both the reflected and transmitted beams are also relatively symmetrical. This symmetry is evident in Fig. 11, illustrated by the evenly spaced contours. This reaffirms the strong dependence of the phase on the thicknesses of the coating layers. In the same manner, in the case of a second-order polynomial, the resulting phase error maps display a second-order form, resembling the shapes of the individual coating layers, as shown in Fig. 12. In both cases of thickness gradients, the range of phase errors is consistently narrower for the transmitted beam compared with the reflected beam, as shown by the PtV values

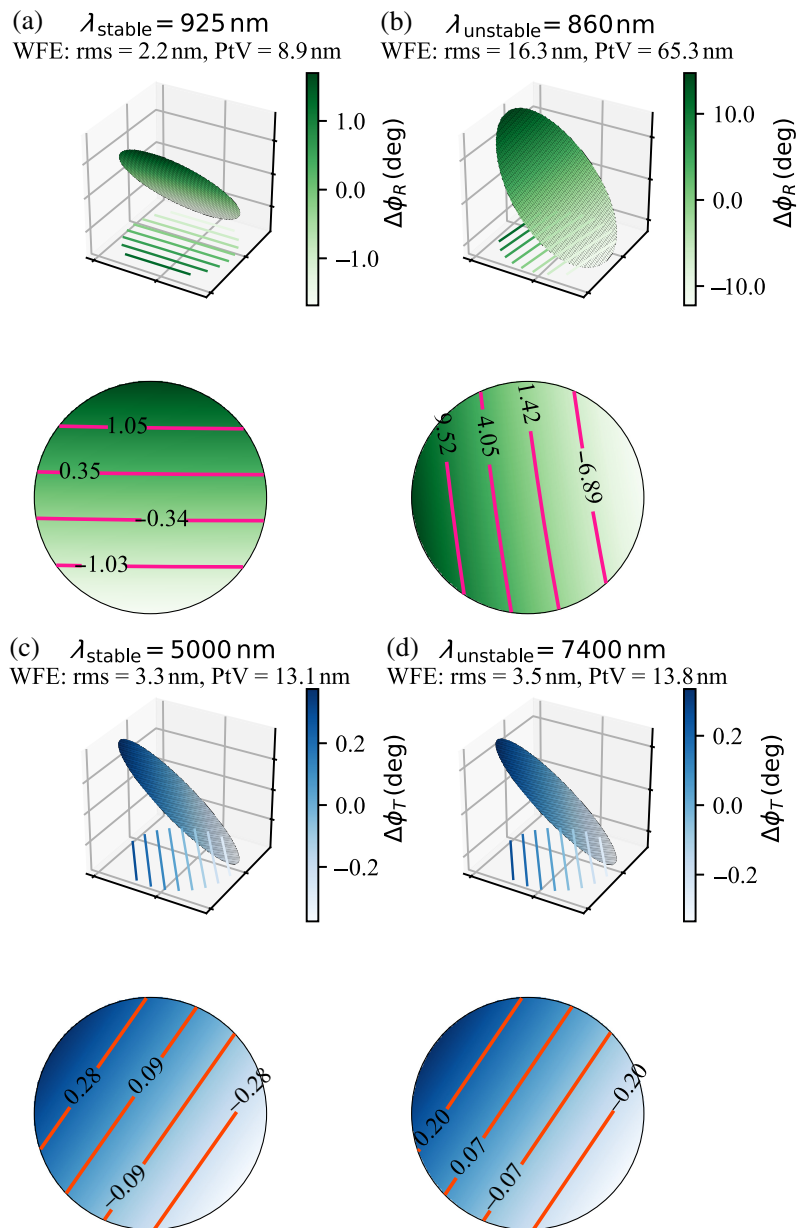


**Fig. 11** First-order gradient as a three-dimensional phase map for the 330 mm  $\times$  330 mm disk representing D1. Plots in green show the case of the reflected beam, and plots in blue show the case of the transmitted beam. The three-dimensional maps of the phase include contours indicated at the base of the plots, whereas their respective two-dimensional phase error maps with contours are shown beneath the three-dimensional plots. The phase errors for stable and unstable wavelength points in the spectrum are indicated using panels (a) and (c) and panels (b) and (d), respectively. The respective rms and PtV WFEs are included for each phase map.

in Figs. 11 and 12. Moreover, there is a significant discrepancy for both reflection and transmission among the wavelengths at which the spectral performance is stable and at points where it is unstable. At wavelengths where the spectrum remains stable without notable features, the phase errors remain small. Conversely, where the spectrum exhibits fringes and other fluctuations, the phase errors become more pronounced. Both the rms and PtV values for the unstable wavelengths are consistently higher in comparison with the stable regions. These features stem from interference effects within the coating layers and are exacerbated by imperfections or changes in the optimized layer thicknesses. The coatings have been optimized to yield a performance that meets the requirements of D1. Any deviations from this recipe will lead to a sub-optimal spectral response.

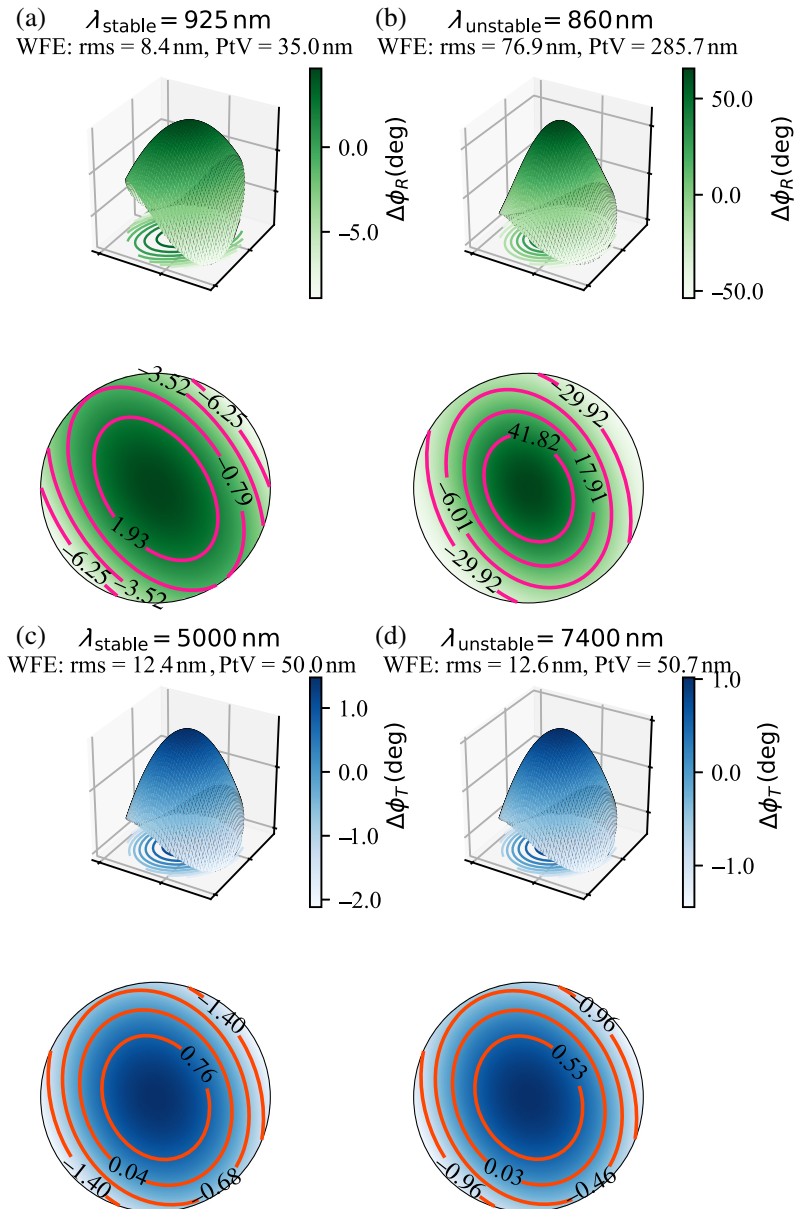


**Fig. 12** Second-order gradient as a three-dimensional phase map for the 330 mm  $\times$  330 mm disk representing D1. Plots in green show the case of the reflected beam, and plots in blue show the case of the transmitted beam. The three-dimensional maps of the phase include contours indicated at the base of the plots, whereas their respective two-dimensional phase error maps with contours are shown beneath the three-dimensional plots. The phase errors for stable and unstable wavelength points in the spectrum are indicated using panels (a) and (c) and panels (b) and (d), respectively. The respective rms and PtV WFEs are included for each phase map.

### 3.6 Photometric Observations: FGS2

The oversampled photometer focal plane of FGS2 when observing the target HD 209458 is depicted in Fig. 13. The image represents the spatial distribution of the detector signal as a result of the co-added PSFs at each wavelength within the FGS2 waveband to create the final photometric images for each source. The PSF, modeled using PAOS, was imported into ExoSim 2.0 to produce the FGS2 detector images. Thus, both the  $x$ - and  $y$ -directions denote spatial directions. As with the spectral images, these simulations exclude detector noise and zodiacal light, meaning all the generated photometric images inherently have no background signal. Thus, the total photometric signal can be found unambiguously by summing the signal of all the subpixels in the

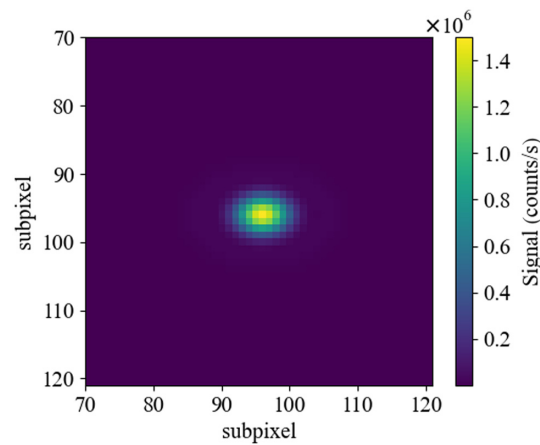


**Fig. 13** Simulated nominal image of the detector of the FGS2 photometer for HD 209458, zoomed into the PSF at the center. The focal plane is oversampled by a factor of 3 to allow for precise centroiding.

detector image. The FGS2 detector image of HD 209458 pictures a maximum signal per second of  $5.2 \times 10^7$  counts/s.

### 3.6.1 Changes in derived centroid position

Although photometric measurements of the stellar target will be acquired in visible wavebands for scientific study, the other primary functionality of the FGS2 channel, alongside FGS1, is the centering, focusing, and guiding of the ARIEL spacecraft. The guidance relies on light from the host star that has traversed the ARIEL optical chain to the FGS2 focal plane to ascertain changes in the line of sight of the satellite in the form of pointing fluctuations. The guiding information of the centroid position of the target star is delivered at a rate of 10 Hz to monitor the pointing stability of the spacecraft.

In this section, two different methods were employed to obtain an estimate of the centroid position. The first method involves the fitting of a two-dimensional Gaussian surface to the image of the FGS2 detector. The other method, instead, finds the intensity-weighted mean position by calculating the mean pixel positions in both the  $x$ - and  $y$ -directions of the photometric image, with each pixel weighted by the measured count rate. Figure 13 depicts the resulting photometric image under the assumption of a uniform phase across the D1 surface. Table 1 and Fig. 14 summarize the change in these centroid positions computed by the two methods when incorporating the WFE maps of D1 using PAOS and ExoSim 2.0, considering both a first and second-order polynomial gradient.

In both methods, the centroid shifts from its original position for the first- and second-order low-spatial frequency error forms, respectively, due to changes in the PSF introduced by the WFE of D1. The WFE introduced by the first-order thickness gradient mirrors the shape of the gradient itself across the various wavelengths within the FGS2 waveband. This has resulted in a slight tilt in the PSF at the focal plane of FGS2, causing a shift in the calculated centroid position.

**Table 1** Change in subpixels of inferred PSF centroids on the focal plane of FGS2, due to the first- and second-order thickness gradient, estimated using two different methods: calculating an intensity-weighted centroid or the centroid of a Gaussian fitted to the PSF.

	Intensity-weighted centroid		Gaussian fit centroid	
	$\Delta X$	$\Delta Y$	$\Delta X$	$\Delta Y$
LSF error				
First order	0.0118	0.0201	0.0106	0.0176
Second order	-0.0010	-0.0004	-0.0011	-0.0005

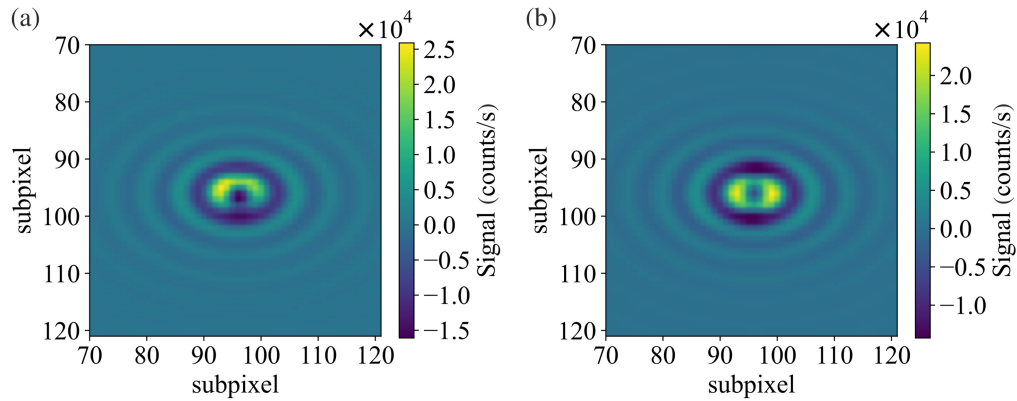


**Fig. 14** Residual of images of FGS2 focal plane between the case of ideal deposition and form errors in deposition for both first (a) and second (b) orders, zoomed into the PSF at the center. The focal plane is oversampled by a factor of 3 to allow for precise centroiding.

The Gaussian-fitted centroid is less sensitive to a shifted position than the intensity-weighted centroid as a result of the tilted PSF. On the other hand, the second-order polynomial thickness error in the D1 coating layers yields a small overall centroid change. This arises as a result of the WFE introduced by D1 being more symmetrical from the central axis of the D1 surface plane. Consequently, it introduces a WFE symmetrical about the central axis of the plane, and thereby near the center of the PSF, leading to a negligible shift in the computed centroid position. The Gaussian fitted centroid records a greater shift for the second-order thickness error in the D1 coating layers, as a second-order WFE results in a PSF that is no longer a well-behaved Airy disk. As such, the Gaussian fitting method struggles to provide an accurate fit for the aberrated PSF.

## 4 Conclusion

The methodology outlined in this article is able to obtain estimates of the levels of phase and wavefront errors at given wavelengths for a multilayer system. Although the application of this has been focused on the ARIEL D1 dichroic, due to the generality of the effects presented here, the findings of this study hold relevance to any instrument that relies on the use of dichroic filters. This can be used to assess the criticality of non-uniform coating layer thicknesses to the desired phase uniformity of the transmitted and reflected beams and, thus, the ability of the component to agree with any phase variation requirements. An accurate physical model of the relevant deposition process used for the coatings can provide the physical distribution of the thickness errors across the dichroic surface. Subsequently, a more accurate map of the phase and wavefront errors can be simulated.

A strong correlation between the variations in the coating layer thicknesses and the phase errors was found. The extent of phase errors remained largely symmetric around the nominal phase and scale linearly with the amplitude of the errors in thickness for both the reflected and transmitted beams. This is a direct result of the thickness errors affecting the overall optical path difference traversed by light. In addition, a clear link has been established between the performance stability at a given wavelength and the resulting phase errors. Notably, abrupt changes in observed phase errors align with wavelengths where interference fringes and spectral variations are prominent in the reflectance and transmittance of the dichroic. These wavelengths were more sensitive to variation in the thicknesses because the designed recipe of thicknesses has been adjusted to yield an optimized spectral performance. This results in a heightened sensitivity of phase errors to thickness variations at these particular wavelengths. The consequent changes in the deduced centroid position of the PSF at the FGS2 focal plane are minimal but heavily dependent on the magnitudes of the thickness error slopes of the coating layers.

Moreover, although higher-order polynomials can be readily modeled, this paper only focused on the first- and second-order forms resulting from gradient depositions and a rotating substrate within the vacuum chamber. Any higher-order forms require justification based on the physical processes that may cause them to form during the deposition of the coating stack.

Nonetheless, this does not imply that such surface forms will not be observed. However, rather than arising directly from the deposition process, such forms are more likely to be attributed to the surface form of the substrate prior to deposition. Such errors can thus be mitigated by imposing stringent requirements on the initial form of the substrate.

Thickness errors also lead to deviations in the spectral performance from the nominal case. The extent and wavelength dependence of these effects on the spectrum of the dichroic depend on the nature and magnitude of the thickness errors. Thurairethinam et al.<sup>11</sup> explore how variations in the coating layer thicknesses, even for uniform and parallel-facing surfaces, impact the nominal performance of the dichroic. It was shown that the interference behavior of the coating is highly sensitive to the layer thicknesses, with the most prominent deviations from the nominal spectral performance occurring at the transition wavelength region. Unlike the areas of maximum transmission and reflection, where the focus of the design remains on optical efficiency, the primary concern in the transition region is its precise location within the waveband. As such, any changes in the original thicknesses will result in a deterioration of the performance and a shift in the transition wavelength.

It should also be noted that environmental changes during the operation of the component may also influence the observed phase. Changes in the angle of incidence directly impact the total optical path difference as a result of a change in the geometrical distance that the beam will traverse within the coating layers and the substrate. Ultimately, this alters the phase of the outgoing beams, as described by Eq. (8), which can also be applied to each of the individual coating layers, as well as the substrate. Similarly, fluctuations in the operating temperature of the system result in changes in the phase of the outgoing beams of the dichroic due to the temperature dependence of the refractive indices of both the coating and substrate materials. Such refractive index variations lead to a modified optical path length and hence introduce deviations in the observed phase of the outgoing beams of the optical component. In addition, information on the effects of environmental changes on the intensity of the outgoing beams and relevant spectral effects can be found in Thurairethinam et al.<sup>11</sup>

---

## Disclosures

The authors declare that there are no financial interests, commercial affiliations, or other potential conflicts of interest that could have influenced the objectivity of this research or the writing of this paper.

## Code and Data Availability

The code used in this study can be found on GitHub at <https://github.com/vinthurai/ASTRALIS>, <https://github.com/arielmission-space/PAOS> and <https://github.com/arielmission-space/ExoSim2-public>.

## Acknowledgments

This work was funded by the Science and Technology Facilities Council (STFC) and the UK Research and Innovation (UKRI).

## References

1. J. P. Gardner et al., “The James Webb Space Telescope mission,” *Publ. Astron. Soc. Pac.* **135**(1048), 068001 (2023).
2. M. Wells, G. Hawkins, and G. Olofsson, “The design and fabrication of multiple dichroic beamsplitters for the miri spectrometer (4.8 – 29  $\mu\text{m}$ ),” *Proc. SPIE* **5487**, 794–803 (2004).
3. O. H. Siegmund et al., “The GALEX mission and detectors,” *Proc. SPIE* **5488**, 13–24 (2004).
4. B. T. Sullivan and J. A. Dobrowolski, “Deposition of metal/dielectric multilayer filters,” *Proc. SPIE* **2253**, 1213–1217 (1994).
5. B. T. Sullivan and J. Dobrowolski, “Deposition error compensation for optical multilayer coatings. I. Theoretical description,” *Appl. Opt.* **31**(19), 3821–3835 (1992).
6. L. M. G. Venancio et al., “Coating induced phase shift and impact on Euclid imaging performance,” *Proc. SPIE* **9904**, 99040V (2016).
7. M. A. Quijada et al., “Spectral and wavefront error performance of WFIRST/AFTA bandpass filter prototypes,” in *IEEE Aerosp. Conf.*, IEEE, pp. 1–12 (2016).

8. B. Cromeey, R. VonHandorf, and J. Sullivan, "Simulations for the performance of the wide field instrument on the Roman Space Telescope," in *IEEE Aerosp. Conf. (AERO)*, IEEE, pp. 1–7 (2022).
9. J. Archer et al., "The 2020 SPICA telescope preliminary design and predicted performance," *Proc. SPIE* **11443**, 1144327 (2020).
10. G. Tinetti et al., "ARIEL: enabling planetary science across light-years," arXiv:2104.04824 (2021).
11. V. Thurairethinam et al., "Monte Carlo transmission line modelling of multilayer optical coatings for performance sensitivity of a dichroic filter for the ARIEL space telescope," *Proc. SPIE* **12180**, 1218048 (2022).
12. A. Ribeaud et al., "Infra-red multi-layer coatings using YbF<sub>3</sub> and ZnS in an ion beam sputtering system," in *Opt. Interference Coat.*, Optical Society of America, p. MC-7 (2019).
13. A. Kotha and J. E. Harvey, "Scattering effects of machined optical surfaces," *Proc. SPIE* **2541**, 54–65 (1995).
14. J. E. Harvey et al., "Total integrated scatter from surfaces with arbitrary roughness, correlation widths, and incident angles," *Opt. Eng.* **51**(1), 013402 (2012).
15. G. Rusu et al., "Structural characterization and optical properties of ZnSe thin films," *Appl. Surf. Sci.* **253**(24), 9500–9505 (2007).
16. D. Stearns, "Stochastic model for thin film growth and erosion," *Appl. Phys. Lett.* **62**(15), 1745–1747 (1993).
17. Y. Wang et al., "Optical properties and residual stress of YbF<sub>3</sub> thin films deposited at different temperatures," *Appl. Opt.* **47**(13), C319–C323 (2008).
18. D. Nečas et al., "Measurement of thickness distribution, optical constants, and roughness parameters of rough nonuniform ZnSe thin films," *Appl. Opt.* **53**(25), 5606–5614 (2014).
19. L. V. Mugnai et al., "ExoSim 2: the new exoplanet observation simulator applied to the Ariel space mission," *Exp. Astron.* **59**(1), 9 (2025).
20. B. Edwards et al., "An updated study of potential targets for Ariel," *Astron. J.* **157**(6), 242 (2019).
21. T. Boyajian et al., "Stellar diameters and temperatures—VI. High angular resolution measurements of the transiting exoplanet host stars HD 189733 and HD 209458 and implications for models of cool dwarfs," *Mon. Not. R. Astron. Soc.* **447**(1), 846–857 (2015).
22. A. Bocchieri, L. V. Mugnai, and E. Pascale, "PAOS: a fast, modern, and reliable Python package for physical optics studies," *Proc. SPIE* **13092**, 130924K (2024).

**Vinooja Thurairethinam** is an optical engineer at the UK Astronomy Technology Centre focusing on the Laser Interferometer Space Antenna and the ArmazoNes High Dispersion Echelle Spectrograph. She obtained her PhD in the Astrophysics Group at University College London (UCL). Her PhD research focused on optical modeling techniques for the dichroic filters used in the ARIEL Space Mission, particularly on the effects of potential systematics on the spectral performance of these optical components, impacting the precision of the spectroscopic observations of the ARIEL mission.

**Andrea Bocchieri** is a postdoctoral researcher. He focuses on the characterization of exoplanet atmospheres with ARIEL. He has experience with atmospheric retrievals, end-to-end instrument simulators, calibration, detrending, and performance studies of the ARIEL mission, as well as his role as ARIEL's telescope scientist.

**Giorgio Savini** obtained his master's in physics and PhD in astronomy at the University of Rome "La Sapienza" (Italy). Following this, he served on the Planck Satellite High Frequency Instrument and the Herschel Space Observatory at Cardiff University (UK). Since its launch in 2009, he joined UCL, where he holds a professorship in astrophysics specializing in infrared astrophysics and instrumentation. Giorgio Savini is currently a payload scientist on the ARIEL Space Mission (ESA) and UK Calibration Convener for Litebird (JAXA). He co-authored more than 260 papers in both physics and astronomy. His main interests are the design and build of metamaterial-based optics for satellite instrumentation and the design of instrumentation for satellite payloads.

**Lorenzo V. Mugnai** is a postdoctoral research associate at Cardiff University, focusing on exoplanet characterization, advancing comparative planetology, and exploring planetary populations. He has contributed to missions such as ARIEL and EXCITE, leveraging tools such as ExoRad and ExoSim to prepare space missions, optimize their design for scientific objectives, predict performance, and prepare data analysis.

**Enzo Pascale** has over 20 years of experience in designing, implementing, operating, and analyzing data from astronomical instruments deployed on space and suborbital platforms, spanning microwaves to visible wavelengths. Since 2010, his research has focused on the spectroscopic characterization of exoplanetary atmospheres using transit spectroscopy from the visible to mid-infrared.